FRANK J. SEILER RESEARCH LABORATORY

SRL-TR-72-0008

MAY 1972

AD743002

# BASE MOTION ISOLATION OF A 2-AXIS BEAM DEFLECTOR

Capt Gary C Comfort

D D C
RECEIVED
JUN 9 1972
B

PROJECT 7904

[redacted]

APPROVED FOR PUBLIC RELEASE;
DISTRIBUTION UNLIMITED.

AIR FORCE SYSTEMS COMMAND
UNITED STATES AIR FORCE

UNCLASSIFIED

Security Classification

## DOCUMENT CONTROL DATA - R & D

*(Security classification of title, body of abstract and indexing annotation must be entered when the overall report is classified)*

| | |
|---|---|
| 1. ORIGINATING ACTIVITY *(Corporate author)*<br>Frank J. Seiler Research Laboratory (AFSC)<br>USAF Academy, Colorado 80840 | 2a. REPORT SECURITY CLASSIFICATION<br>Unclassified<br>2b. GROUP |

3. REPORT TITLE

Base Motion Isolation of a Two-Axis Beam Deflector

4. DESCRIPTIVE NOTES *(Type of report and inclusive dates)*

Scientific Report

5. AUTHOR(S) *(First name, middle initial, last name)*

Gary C. Comfort, Capt, USAF

| | | |
|---|---|---|
| 6. REPORT DATE<br>May 1972 | 7a. TOTAL NO. OF PAGES<br>18 | 7b. NO. OF REFS<br>7 |
| 8a. CONTRACT OR GRANT NO.<br>b. PROJECT NO. 7904-00-40<br>c. DRS 61102F<br>d. BPAC 681304 | 9a. ORIGINATOR'S REPORT NUMBER(S)<br>SRL-TR-72-0008<br>9b. OTHER REPORT NO(S) *(Any other numbers that may be assigned this report)*<br>DDC #AD | |

10. DISTRIBUTION STATEMENT

Approved for public release; distribution unlimited.

| | |
|---|---|
| 11. SUPPLEMENTARY NOTES | 12. SPONSORING MILITARY ACTIVITY<br>Frank J. Seiler Research Laboratory (AFSC)<br>USAF Academy, Colorado 80840 |

13. ABSTRACT

The base motion isolation characteristics of an optical beam deflector with a two-axis gimbal support are investigated. The particular configuration of the beam deflector system considered utilizes rate integrating gyros to provide a rate inner control loop with an optical tracker providing an outer position control loop. Base motion isolation is partially achieved by the gimbal support assumed to be frictionless. However, input beam motion relative to the optical surface of the beam deflector is shown to produce large excursions of the output beam. As a result, a feed-forward control loop is added to measure and compensate for input beam motion, i.e., base motion. Every effort is directed to use optimistic estimates of beam deflector performance in order to develop a measure of the smallest pointing error possible with such a two-axis beam deflector configuration. The base motion spectrum used is intended to approximate that of a large aircraft in normal flight.

DD FORM 1 NOV 65 1473

UNCLASSIFIED

Security Classification

UNCLASSIFIED

Security Classification

| 14. KEY WORDS | LINK A ROLE | LINK A WT | LINK B ROLE | LINK B WT | LINK C ROLE | LINK C WT |
|---|---|---|---|---|---|---|
| Optical Pointing | | | | | | |
| Beam Deflectors | | | | | | |
| Heliostats | | | | | | |
| Airborne Heliostats | | | | | | |
| Base Motion Isolation of a Heliostat | | | | | | |

UNCLASSIFIED

Security Classification

BASE MOTION ISOLATION OF A

TWO-AXIS BEAM DEFLECTOR

Capt Gary C. Comfort
Research Associate
Frank J. Seiler Research Laboratory
United States Air Force Academy, Colorado 80840
U.S.A.

ABSTRACT

The base motion isolation characteristics of an optical beam deflector with a two-axis gimbal support are investigated. The particular configuration of the beam deflector system considered utilizes rate integrating gyros to provide a rate inner control loop with an optical tracker providing an outer position control loop. Base motion isolation is partially achieved by the gimbal support assumed to be frictionless. However, input beam motion relative to the optical surface of the beam deflector is shown to produce large excursions of the output beam. As a result, a feed-forward control loop is added to measure and compensate for input beam motion, i.e., base motion. Every effort is directed to use optimistic estimates of beam deflector performance in order to develop a measure of the smallest pointing error possible with such a two-axis beam deflector configuration. The base motion spectrum used is intended to approximate that of a large aircraft in normal flight.

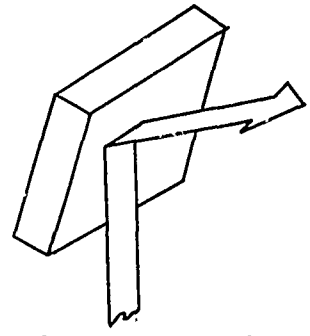

Figure 1. Beam Deflector

## I. INTRODUCTION

Recently applications have arisen which involve the airborne transmission and/or reception of information with optical wavelengths. Many of these applications require a precise optical pointing system to transmit or collect the optical energy. Several configurations of optical surfaces are conceivable for such a purpose. One of the simplest concepts to conceive is that of the optical beam deflector as depicted in Figure 1. In order to provide the capability of directing the optical beam in any direction independent of aircraft altitude, it is necessary to mount the beam deflector in gimbals. The particular gimbal configuration depicted in Figure 2 allows for motion of the beam deflector about two axes. This is the minimum number of gimbals needed to allow motion in both azimuth and elevation.

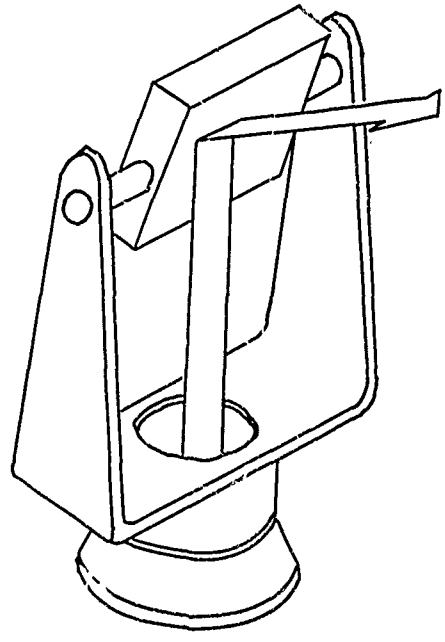

Figure 2. Two-Axis Beam Deflector

Depending upon the specific application of the optical information, the beam deflector may be used either to transmit optical energy from the aircraft to a target or to collect optical energy from an external target source into the aircraft. For some applications two-way transmission of optical energy might be required. For purposes of clarity only, the source of optical energy will be considered to be aboard the aircraft and the beam deflector will have the purpose of directing this energy upon an external target. Thus the input beam will be considered to be the optical energy transmitted from the airborne source to the beam deflector while the output beam will be the optical energy path from the beam deflector to the external target. For applications in which the role of source and target are interchanged the following investigation applies fully with only a change in nomenclature.

The investigation of base motion isolation capability of the particular beam deflector configuration considered herein is intended to:

a) determine the smallest pointing error which could conceivably be obtained from such a configured system operating within an aircraft with the base motion spectrum assumed, and

b) serve as a guide to considering the effects of base motion upon the performance of other airborne optical pointing systems.

## II. BEAM DEFLECTOR CONTROL

In order to discuss quantitatively the control and performance of the two-axis beam deflector, it is necessary to introduce several coordinate systems. These are depicted in Figure 3 as:

I - fixed in inertial space

V - fixed to the vehicle with coordinate axes i, j, k

O - fixed to the outer or azimuth gimbal with coordinate axes n, e, k

M - fixed to the beam deflector with coordinate axes r, e, d

L - line-of-sight coordinates with coordinate axes l, e, p.

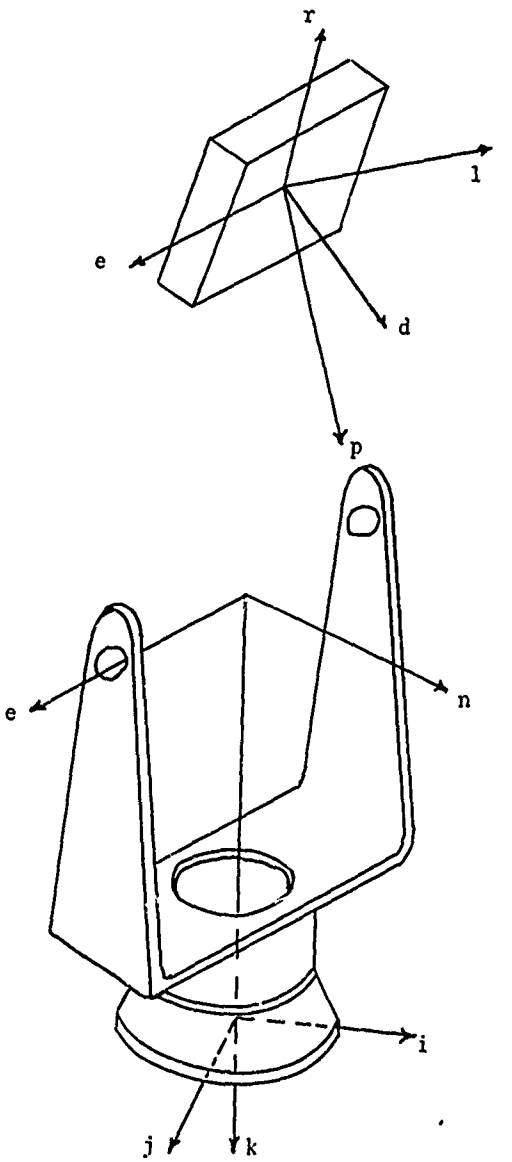

Figure 3. Coordinate Axes

The purpose of the beam deflector control system is to direct the output beam along the desired direction. This is accomplished by controlling the elevation angle ε and the azimuth angle η where η is measured between the base and the outer gimbal and ε is measured between the outer gimbal and the beam deflector surface as shown in Figure 4.

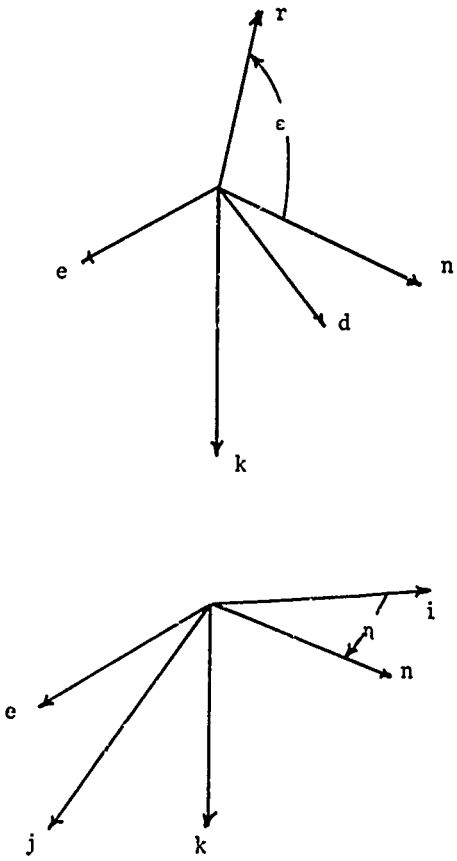


Figure 4. Controlled Angles

The beam deflector control can be accomplished by two control loops, elevation and azimuth. These basic features of these loops are block diagrammed in Figures 5a and 5b.

For the particular configuration of beam deflector considered herein, it is assumed that the input beam source is mounted on the outer gimbal coincident with that gimbal's axis of rotational freedom. For such a configuration, an angular velocity of the outer gimbal and hence the input beam, about the elevation axis, $\omega_{0_e}$, produces a corresponding angular velocity of opposite sign of the output beam direction. This is accounted for in Figure 5a by the disturbance angular velocity, $-\omega_{0_e}$.

A rotation of the mirror surface with respect to the input direction about the e axis is easily seen to produce a rotation of twice that magnitude of the output beam direction. The angular velocity of the output direction about the e axis is thus

$$\omega_{L_e} = 2\omega_{M_e} - \omega_{0_e} \qquad (1)$$

Since the direction to be controlled is that of the output beam, it is desirable to measure the motion of this output direction with a high bandwidth sensor. Unfortunately, the output direction is only a direction in space; it does not correspond to any direction in the physical hardware. Thus there is no way of mounting a sensor on this output beam direction to measure its motion.* Instead motion sensors can only be attached to the gimbals and the vehicle itself. The elevation control loop of Figure 5a postulates the use of a rate integrating gyroscope mounted on the inner gimbal with its input direction along the e axis. The azimuth control loop of Figure 5b utilizes a rate integrating gyroscope mounted on the outer gimbal with its input direction along the k axis. The rate integrating gyros provide a relatively high bandwidth rate-feedback loop about the elevation and azimuth gimbals.

Inasmuch as the measurement of primary interest is the orientation of the output beam with respect to the target, an optical tracker is incorporated in the control system. The tracker is oriented so that the center of its field of view always is coincident with the output beam direction. Thus the tracker measures angles between the output beam direction and the desired target direction. The tracker thus provides an outer position-feedback loop.

The beam deflector is positioned by gimbal torque motors. The commands are input to the torque generator of the rate integrating gyroscope. The output angle of the gyroscope produces the electrical input to the gimbal torque motor.

Figure 5 depicts disturbance torques $T_{d_e}$ and $T_{d_a}$ upon the elevation and azimuth control loops respectively. These torques are dynamic reaction torques arising from the rotation of

---

* Other mechanizations of the two-axes beam deflector are possible in which a slaved platform is driven by the angular velocity of the mirror with a two-to-one gear ratio. The slaved platform body axes then correspond with those of the line-of-sight frame. Measurements of the motion of the slaved platform made by sensors which can be physically attached to it, can thus be used as measurements of the motion of the output beam direction. Such a system has been described elsewhere [1] and is not considered in this investigation.

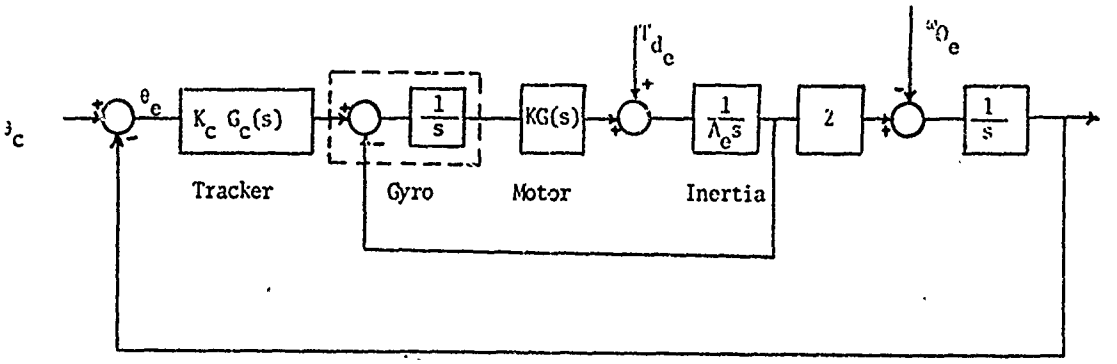


Figure 5a. Basic Elevation Loop

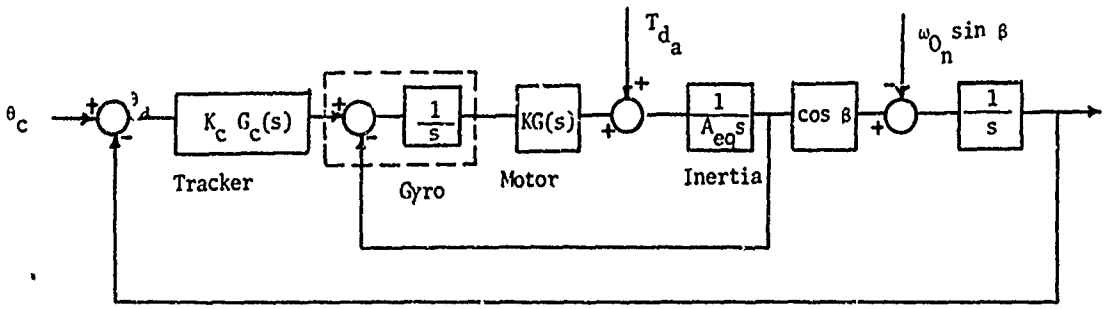


$A_{eq} = B_k + A_r \sin^2 \varepsilon + A_d \cos^2 \varepsilon$ (see Appendix A)

$\beta = \cos(2\varepsilon - \pi/2)$

Figure 5b. Basic Azimuth Loop

the gimbal frames with respect to inertial space. These dynamic torques have been presented elsewhere [2]. Appendix A contains a derivation of the equations of motion for both the elevation and azimuth gimbals including the dynamic reaction torques.

## III. BASIC ELEVATION CONTROL LOOP DESIGN AND EVALUATION

Figure 5a presents a functional block diagram of a basic elevation control loop. In order to evaluate the pointing performance of such a control loop the following representative parameter values were used :

$$K_a = \frac{K}{A_e} = 132000$$

$$G(s) = \frac{(\frac{s}{12} + 1)\ (\frac{s}{67} + 1)}{(s + 1)\ (\frac{s}{402} + 1)}$$

In order to track a target with a constant line-of-sight velocity without a steady state tracking error, a type II control loop is desired. This is obtained by choosing the tracker dynamics as

$$G_c(s) = \frac{(\frac{s}{27} + 1)}{s}$$

The overall loop gain can be adjusted by setting the tracker gain, $K_c$. In order to provide a basis for this choice, a root locus of the control loop with parameter values as given above is presented as Figure 6.

To minimize the effect of the disturbances produced by the dynamic reaction torque and by the base motion, a large value for loop gain is desired. However, as evidenced by Figure 6, too large a value for loop gain will produce an underdamped response which would lead to unacceptable settling following commanded angular slews. Thus a compromise value of loop gain is needed.

The closed loop poles indicated on Figure 6 result from the choice of tracker gain, $K_c$, of 500.

The basic control loop design is thus completed.

To evaluate the effectiveness of the basic control loop design in rejecting undesired disturbances, one must consider the two sources of disturbance: the dynamic torque, $T_{d_e}$, and the input beam motion, $\omega_{0_e}$. Both of these disturbances can be written in terms of the base motion disturbances and the required tracking rate. In functional form

$$T_{d_e} = T_{d_e}\left(\omega_{V_i}^2, \omega_{V_j}^2, \omega_{L_p}^2, \omega_{V_i}\,\omega_{L_p}, \omega_{V_j}\,\omega_{L_p}\right)$$

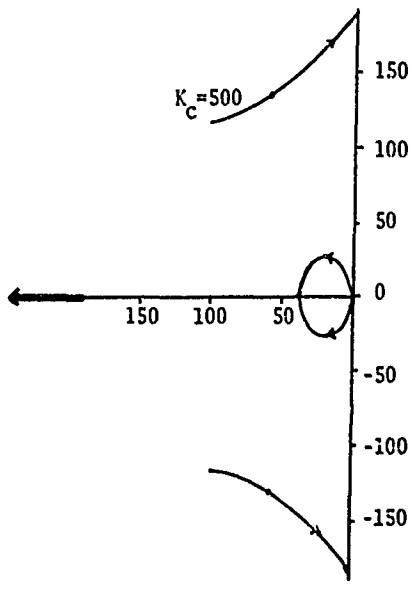


Figure 6. Elevation Root Locus

$$\omega_{0_e} = \omega_{0_e}\left(\omega_{V_i}, \omega_{V_j}\right)$$

where

$\omega_{V_i}$ is the component of base angular velocity along the i direction.

$\omega_{V_j}$ is the component of base angular velocity along the j direction.

$\omega_{L_p}$ is the component of line of sight angular velocity along the p direction.

The angular velocities of the base and line of sight are predictable only as random variables. Thus these may be described statistically in terms of their power spectral density (PSD) functions. The result of the analysis will be the RMS pointing error angle, $\theta_{e_{RMS}}$. Since $\theta_e$ is the output of a linear system having several random disturbance inputs assumed to be statistically independent,

$$\phi_{\theta_e}(\omega) = \sum_{i=1}^{N} \left| \frac{\theta_e}{X_i}(\omega) \right|^2 \phi_{X_i}(\omega)$$

where $\frac{\theta_e}{X_i}(\omega)$ is the performance function relating the ith independent disturbance, $X_i$, to the pointing error, $\theta_e$.

The RMS pointing error is then obtained as

$$\theta_{e_{RMS}} = \left\{ \frac{1}{2\pi} \int_{-\infty}^{\infty} \phi_{\theta_e}(\omega)\, d\omega \right\}^{1/2}$$

In order to carry out the above evaluation procedure, it is necessary to:

a. Write the disturbance inputs in terms of the basic variables of base motion and pointing rates.

b. Determine the PSD of each of these disturbance inputs assuming independence.

c. Determine the performance function relating each of these disturbance inputs to the pointing error angle, $\theta_e$.

Steps a and b above are carried out in Appendix B. Step c is readily accomplished noting from Figure 5a that

$$\frac{\theta_e}{T_{d_e}}(s) = \frac{\frac{1}{K_c G_c}}{\frac{s^3}{2 K_a K_c G G_c} + \frac{s}{2 K_c G_c} + 1}$$

and

$$\frac{\theta_e}{\omega_{0_e}}(s) = -\frac{\frac{1}{2 K_c G_c}\left(\frac{s^2}{K_a G} + 1\right)}{\frac{s^3}{2 K_a K_c G G_c} + \frac{s}{2 K_c G_c} + 1}$$

The PSD chosen to represent aircraft angular velocity about each axis is given as

$$\phi_{\omega_v} = \frac{(0.1)(1400^2)}{(\omega^2 + 1.5^2)(\omega^2 + 1400^2)} \quad \frac{(\text{rad/sec})^2}{\text{hz}} \quad (2)$$

This base motion PSD is plotted as Figure 7.

Using the procedure outlined above the PSD of resulting pointing error for the basic elevation control loop is determined. This PSD is plotted as Figure 8. The RMS pointing error angle is evaluated to be

$$\theta_{e_{RMS}} = 942.8 \ \mu\text{rad}$$

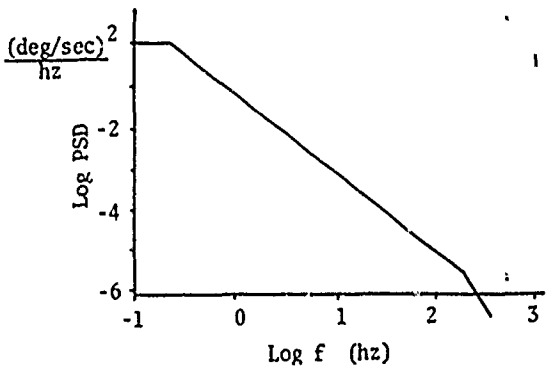


Figure 7. Base Motion PSD

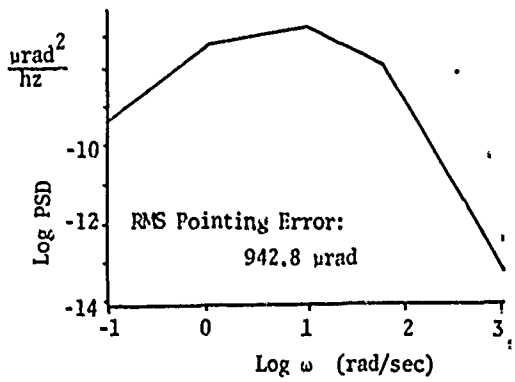


Figure 8. Pointing Error PSD

As evidenced by Figure 5, the pointing error arises due to both dynamic torque disturbance and also due to the angular velocity of the input beam, $\omega_{0_e}$, produced by the base motion. In order to evaluate the relative importance of each of these disturbances, the pointing error resulting from the dynamic torque disturbance alone is evaluated using the above procedures. The RMS pointing error caused by the dynamic torque alone is found to be

$$\theta_{e_{RMS}} \text{ (by dynamic torque)} = 1.8 \ \mu\text{rad}$$

From the above, it is readily concluded that the overwhelming cause of the pointing error determined above is base motion disturbance. For this reason, the dynamic torque disturbance effects will not be considered further.

For most precision pointing applications, the RMS pointing error angle of about 1 milliradian determined above is not acceptable. In order to reduce the pointing error, base motion compensation is evaluated.

## IV. FEED-FORWARD COMPENSATION FOR BASE MOTION

In order to reduce the pointing error caused by the motion of the input beam, i.e., by base motion, a feed-forward compensation scheme is considered. This scheme proposes to add a compensation signal, $X_c$, as a command torque to the rate integrating gyro in the elevation control scheme inner loop. The compensation command must be chosen such that the disturbance of input beam motion, $-\omega_{0_e}$, shown in Figure 5a is effectively cancelled.

Consider the portion of the elevation control loop reproduced from Figure 5a as Figure 9.

In order to determine the proper compensation signal, $X_c$, the performance function of the inner loop must be investigated.

Using the dynamics postulated previously, the open loop performance function of this inner loop is

$$PF_{OL}(s) = \frac{132000\left(\frac{s}{12} + 1\right)\left(\frac{s}{67} + 1\right)}{s^2\,(s + 1)\left(\frac{s}{402} + 1\right)}$$

The resultant closed loop performance function for this inner loop is

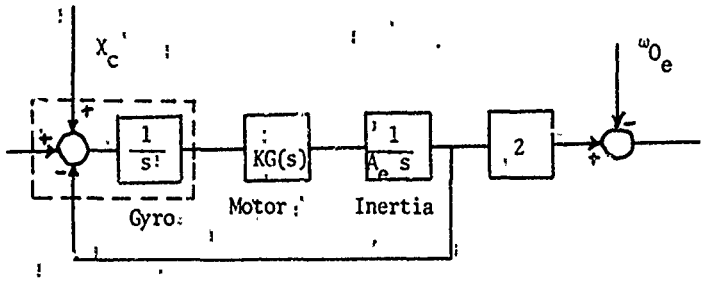


Figure 9. Elevation Inner Loop

$$PF_{CL}(s) = \frac{\left(\frac{s}{12}+1\right)\left(\frac{s}{67}+1\right)}{\frac{s^4}{(402)(132000)}+\frac{403\,s^3}{(402)(132000)}+\frac{s^2}{(12)(67)}+\left(\frac{s}{12}+\frac{s}{67}\right)+1}$$

Inasmuch as the above performance function can be quickly shown to have two real poles, it is easily factored to

$$PF_{CL}(s) = \frac{\left(\frac{s}{12}+1\right)\left(\frac{s}{67}+1\right)}{\left(\frac{s}{11.83726}+1\right)\left(\frac{s}{190.37879}+1\right)\left\{\frac{s^2}{(153.44937)^2}+\frac{2(0.654235)s}{153.44937}+1\right\}}$$

The disturbance caused by input beam motion, $-\omega_{0_e}$, can be eliminated by the addition of a feed-forward compensation signal chosen such that

$$X_c(s) = \frac{0.5}{PF_{CL}(s)}\,\omega_{0_e}(s) = G_{comp}(s)\,\omega_{0_e}(s)$$

The resulting control loop diagram including feed-forward compensation is shown as Figure 10.

Note that for the present it is assumed that a perfect measurement of $\omega_{0_e}$ is available.

Using the compensated control loop of Figure 10, the pointing error angle PSD is again determined. As expected, compensation for base motion is virtually complete with an RMS pointing error of $\theta_{e_{RMS}} = 1.8$ μrad caused by the dynamic torque disturbance remaining.

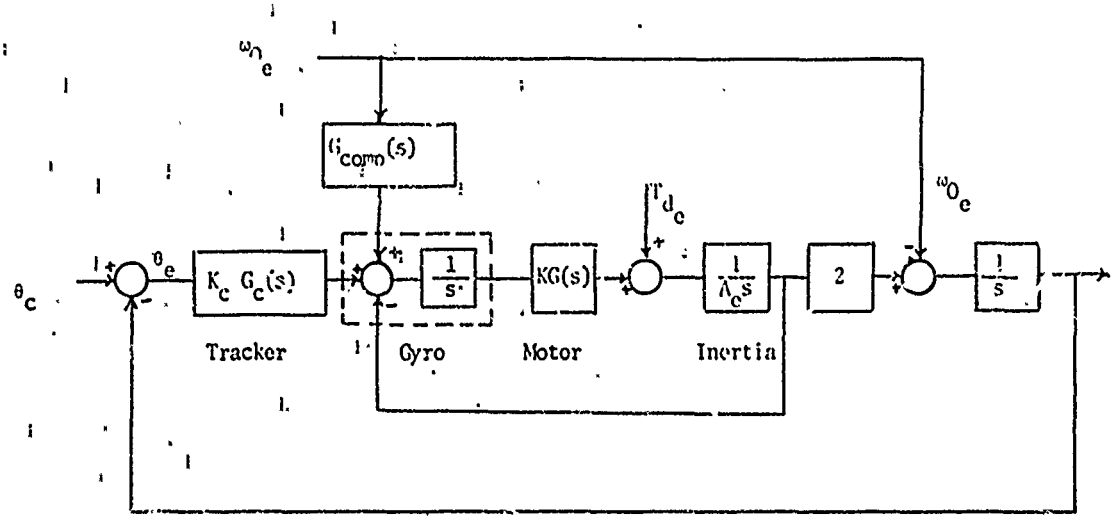


Figure 10. Elevation Loop with Feed Forward

Although the above shows that complete compensation is theoretically possible, one must consider the practical feasibility of determining the locations of poles and zeroes of an actual hardware inner loop in order to construct $G_{comp}(s)$. In reality, one could not determine the locations of singularities to five decimal places as assumed above. The approximate frequency response of the actual inner loop could be determined over the frequencies of interest by exhaustive testing using known inputs. The approximate locations of the singularities could then be determined analytically to match the measured frequency response in a satisfactory manner. The proximity of the singularities determined in such a manner to those of the actual hardware control loop would depend upon many factors including the accuracy with which the experimental measurements are obtained and the skill of the investigator in choosing an analytical function with the correct number and form of poles and zeroes. As a very optimistic estimate of the accuracy of such a procedure, the following "realistic" compensation filter is assumed:

$$G_{comp}(s) = \frac{0.5\left(\frac{s}{190}+1\right)\left\{\frac{s^2}{153^2}+\frac{2(0.7)s}{153}+1\right\}}{\left(\frac{s}{67}+1\right)\left(\frac{s}{5000}+1\right)^2} \qquad (3)$$

The additional poles in the filter are required to keep the gain at high frequency finite.

Using $G_{comp}(s)$ as given by Equation (3) in the block diagram of Figure 10, the pointing error PSD was again determined and is plotted as Figure 11. The RMS pointing error angle was determined to be

$$\theta_{\omega_{RMS}} = 13.1 \text{ urad}$$

It must be emphasized that the above error results even though a perfect measurement of the input beam motion, $\omega_{0_e}$, is assumed. The

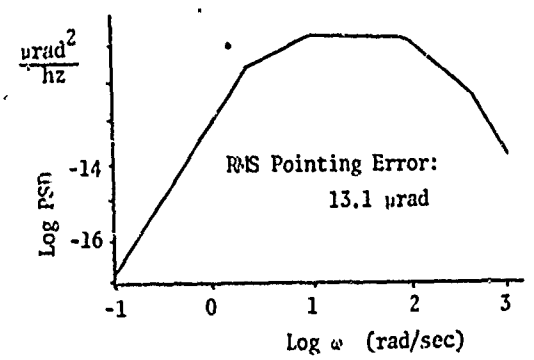


Figure 11. Pointing Error PSD With Feed Forward

error is attributable to the imprecision with which $G_{comp}(s)$ given by Equation (3) approximates the inverse of the closed inner loop function $PF_{CL}(s)$.

The base motion isolation performance of the beam deflector elevation loop will be further degraded for a perfect measurement of input beam motion, $\omega_{0_e}$, is not possible. In reality, such a quantity must be measured by a physical sensor which will add both dynamics and noise.

In order to provide a highly accurate measurement of $\omega_{0_e}$, a rate integrating gyro will be used. By providing a constant gain feedback loop around such a gyro, the electronic analog of a mechanical rate gyro is created without the mechanical problems usually associated with rate gyros.

The output of a rate integrating gyro is characterized by [3]

$$A_g = \frac{1}{\tau_g s+1}\left\{\frac{H_s}{c_g}\frac{1}{s}\left[\omega_{IA}-\omega_{CMD}-A_g\omega_{SRA}+(\nu)\omega_g\right]-\tau_g\omega_{OA}\right\} \qquad (4)$$

where

$A_g$ = output angle of the gyro

$\tau_g = \frac{I_g}{c_g}$ = gyro characteristic time

$H_s$ = gyro spin angular momentum

$c_g$ = gyro damping

$\omega_{IA}$ = angular velocity along the input axis

$\omega_{OA}$ = angular velocity along the output axis

$\omega_{CMD}$ = commanded angular velocity

$(\nu)\omega_g$ = gyro drift rate uncertainty (i.e., noise)

Since the gyro is to be used in a feedback mode, $A_g$ will remain very small. In addition, for simplicity of analysis, cross-axis coupling will be neglected for the present. Thus the rate integrating gyro equation is approximately

$$A_g = \frac{\frac{H_s}{c_g}}{(\tau_g s+1)s}\left[\omega_{IA}-\omega_{CMD}+(\nu)\omega_g\right]$$

To use the gyro as an electronic equivalent of a conventional rate gyro, the command angular velocity is made proportional to $A_g$. Figure 12 presents a block diagram of such an arrangement.

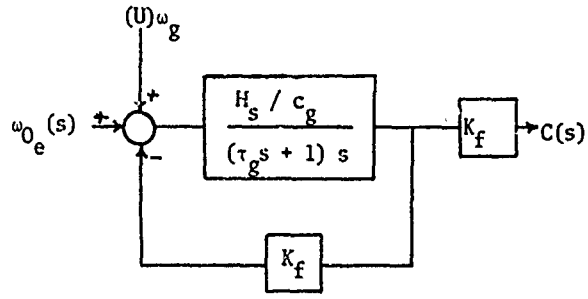


Figure 12. Gyro Block Diagram

Note that the output is obtained by a final multiplication by gain $K_f$ to insure a unity steady state gain.

The measurement loop output, C(s), is related to the desired input $\omega_{0_e}(s)$, by

$$G_{gyro}(s) = \frac{C(s)}{\omega_{0_e}(s)} = \frac{1}{\frac{\tau_g c_g}{H_s K_f} s^2 + \frac{c_g}{H_s K_f} s + 1}$$

The parameters for the rate integrating gyro used to measure $\omega_{0_e}$ are chosen to be representative and correspond to those for a Kearfott King Series miniature rate integrating gyro model C70 2519 001 [4]. The parameter values are

$$\frac{H_s}{c_g} = 15$$

$$\tau_g = 0.006 \text{ seconds}$$

The choice of feedback gain, $K_f$, about this rate integrating gyro is of necessity a compromise. A high gain produces a desired increase in natural frequency but at the expense of a decrease in damping ratio. A compromise choice of $K_f = 15$ is made. This choice results in a natural frequency of 193.6 rad/sec for the second order dynamics of the rate measurement with a damping ratio of 0.43.

Since the designer is aware that the rate measurement process involves second order dynamics, he can attempt to modify his compensation filter, $G_{comp}(s)$, to partially compensate for the measurement dynamics as well as the dynamics of the inner control loop. Again, since the dynamics of the gyro measurement loop are not known exactly, the feed-forward compensation filter might optimistically be chosen as

$$G_{comp}(s) = \frac{0.5\left(\frac{s}{190}+1\right)\left\{\frac{s^2}{153^2}+\frac{2(0.7)s}{153}+1\right\}\left\{\frac{s^2}{194^2}+\frac{2(0.4)s}{194}+1\right\}}{\left(\frac{s}{67}+1\right)\left(\frac{s}{5000}+1\right)^4} \quad (5)$$

where again additional poles have been added to provide finite high frequency gain, i.e., a physically realizable filter.

Using the above filter, the overall block diagram of the elevation axis control loop is shown in Figure 13.

With $G_{comp}(s)$ given by Equation (5) the block diagram of Figure 13 was used to determine the pointing error PSD for the elevation axis control loop. Assuming no gyro noise in the rate measurement loop, the RMS pointing error was determined as

$$\theta_{e_{RMS}} = 29.2 \ \mu\text{rad}$$

Thus it is apparent that the ability of the feed-forward signal to compensate for input beam motion is somewhat degraded by the addition of measurement dynamics.

It should be noted, however, that the measurement dynamics are a function of the specific sensor selected. Rate integrating gyroscopes are available with characteristic times, $\tau_g$, an order of magnitude smaller than that used in the above calculations [5]. The usefulness of such additional response is determined by the required pointing accuracy for a specific mission.

In addition to dynamics, an actual sensor used to measure input beam motion, $\omega_{0_e}$, can be

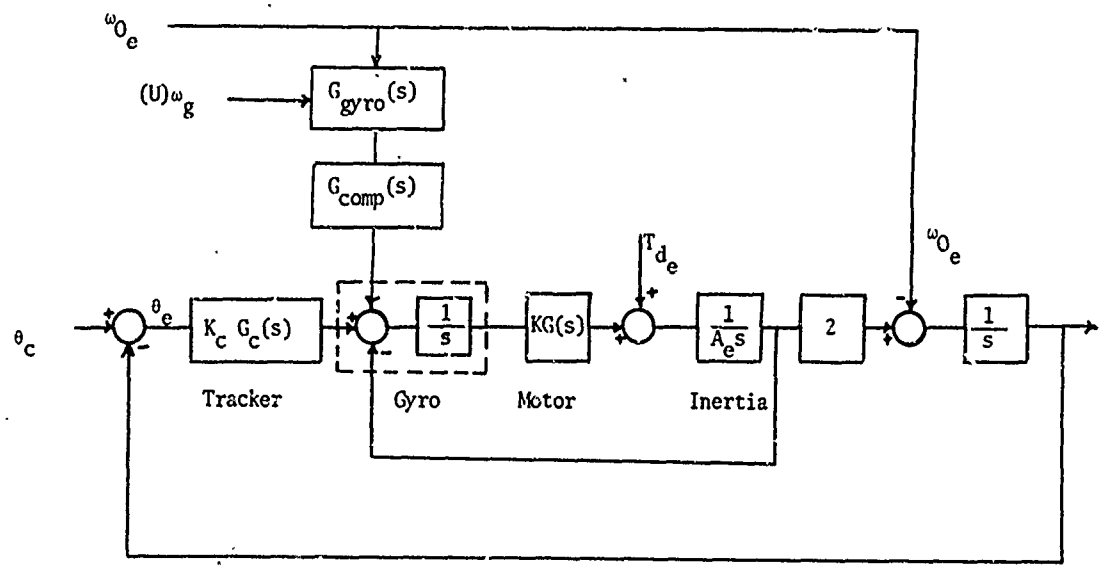


Figure 13. Overall Elevation Loop

expected to add measurement noise. Adequate test measurements upon a representative integrating gyro to determine its noise output across the frequency spectrum of interest are very scarce. A noise model PSD for a Honeywell gyro model CG159C1 has been reported as [6]

$$\phi(f) = \frac{10^{-10}}{f^2}\left\{1 + \left[\frac{f}{10^{-3}}\right]^2\right\}(1+f^2)\ \frac{(\text{deg/hr})^2}{\text{hz}}$$

Assuming the gyro noise to be uncorrelated with all other disturbances, the performance of the elevation control loop was again evaluated using the above gyro noise PSD. The RMS pointing error caused by gyro noise alone was determined to be

$$\theta_{e_{RMS}}\ (\text{gyro noise}) = 0.19\ \mu\text{rad}$$

Recently, information on the noise PSD's of several high quality gyroscopes has been published [5]. The noise is presented in terms of equivalent input angle in $\frac{\text{arcsec}^2}{\text{hz}}$. Across a spectrum of 0.01 hz to 100.00 hz, several of the tested gyros are shown to possess RMS uncertainties of less than 0.05 arcsec of input angle. This is consistent with the RMS pointing error determined above and indicates that short term gyro noise is an unlikely source of significant error in the operation of precision optical directors.

## V. AZIMUTH LOOP DESIGN

The basic azimuth loop of Figure 5b is redrawn as Figure 14. It is seen that the rotation of the pointing direction about the p axis results not only from rotations about the k axis which are controlled but also from rotations about the n axis. Inasmuch as the controlled direction has no gimbal isolation from the base about the n axis, rotations of the base about this axis produce rotational disturbances of the line-of-sight.

In a manner analogous to that described in the preceding sections, a feed-forward path can be added to reduce the effect of base motion. Such a loop is shown in Figure 15. The angular acceleration of the base about the n axis is measured and provided as a command torque to the azimuth torque motor.

The performance function for the angular accelerometer corresponds to that measured for a Systron-Donner Model 4590-F-1-AG angular accelerometer [7].

As with the elevation control loop, a filter is added to compensate for the measured dynamics of the control loop and of the angular accelerometer. Again, the matching of the filter to the actual dynamics is chosen to be an optimistic estimate of that which could be attained.

Using the base motion PSD of Equation (2) and the above control loop, the PSD of azimuth pointing error about the p axis is determined. The RMS value of this pointing error produced by base motion is found to be

$$\theta_{p_{RMS}} = 14.2\ \mu\text{rad}$$

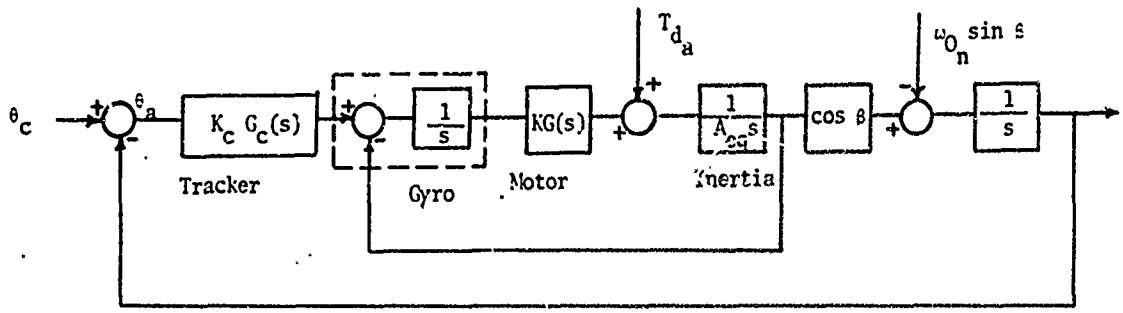


$A_{eq}=B_k+A_r\sin^2\varepsilon+A_d\cos^2\varepsilon$ (see Appendix A)

$\beta = \cos(2\varepsilon - \pi/2)$

Figure 14. Basic Azimuth Loop

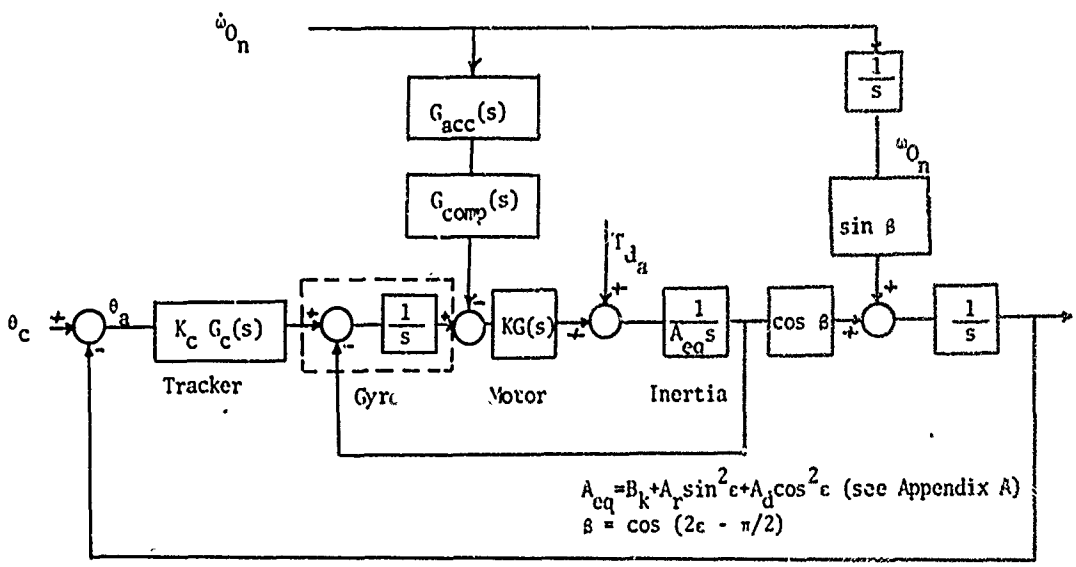


$A_{eq}=B_k+A_r\sin^2\varepsilon+A_d\cos^2\varepsilon$ (see Appendix A)

$\beta = \cos(2\varepsilon - \pi/2)$

Figure 15. Azimuth Loop With Feed Forward

## VI. ADDITIONAL CONSIDERATIONS

In an attempt to assess the minimum pointing error which might be attainable with an airborne two-axis beam deflector of the design considered, several complications have been neglected. These include gyro output axis cross-coupling, gimbal bearing friction, and gimbal non-rigidity.

As indicated by Equation(4), an angular velocity of the gyro case about its output axis will produce an output signal from the gyro which is not desired. In the control loop presented for elevation axis control, it is assumed

that a single degree of freedom, rate integrating gyro is affixed to the beam deflector with its input axis aligned along the e axis. The azimuth control loop assumes a similar gyro mounted on the outer gimbal with its input axis along the k direction. In order to avoid output axis coupling between the loops, the output axis of this azimuth gyro can be aligned with the n direction. On the other hand, the output axis of the elevation gyro must lie in a plane containing the k direction. Hence controlled angular velocities of the azimuth loop about the k axis will produce an erroneous output of the elevation gyro due to its output axis coupling. This coupling is diagrammed in Figure 16. Although such coupling provides an unwanted disturbance, it does not alter the loop stability.

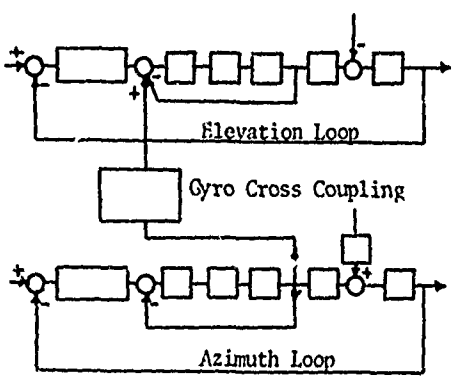


Figure 16. Gyro Cross Coupling Between Loops

In addition angular velocities of the base about the n direction provide erroneous outputs from both the azimuth and elevation loop gyros due to output axis coupling.

The effect of output axis coupling can be reduced by compensation. For example, recognizing that angular velocities about the n and k axes will couple to the elevation control loop gyro, one can measure these angular velocities with appropriate gyros. Knowing the characteristic time of the elevation gyro, a compensating command torque can be provided to compensate for the unwanted output axis coupling.

In addition to the effect of gyro cross-axis coupling, the problems of gimbal bearing friction and gimbal non-rigidity have not been included in this analysis. These effects could alter the natural frequencies and stability of the loops. Each of these neglected effects can be expected to increase the pointing errors. The amount of degradation of loop performance could depend upon the specific mechanical design of both the beam deflector and its gimbals.

## VII. RESULTS

For the control loop design and base motion spectrum considered in this investigation, the RMS pointing error for the cases considered is summarized as follows:

ELEVATION LOOP

| | $\theta_{e_{RMS}}$ in μrad |
|---|---|
| 1. No feed-forward compensation | 942.8 |
| 2. Feed-forward compensation*. Perfect measurement of $\omega_{0_e}$ | 13.1 |
| 3. Feed-forward compensation*. Gyro 2nd order dynamics in measuring $\omega_{0_e}$**. | 29.2 |
| 4. Feed-forward compensation. Gyro 2nd order dynamics* and gyro noise in measuring $\omega_{0_e}$ | 29.2 |

AZIMUTH LOOP

| | $\theta_{p_{RMS}}$ in μrad |
|---|---|
| Feed forward compensation.* Accelerometer 2nd order dynamics in measuring $\dot{\omega}_{0_n}$. | 14.2 |

## VIII. CONCLUSIONS

1. The use of feed-forward compensation can significantly reduce the pointing error caused by base motion of an airborne two-axis beam deflector.

2. The resulting pointing error depends upon the degree with which hardware dynamics can be measured and matched.

---

* Feed forward compensation includes "optimistic" matching of control loop dynamics.

** Effect of gyro dynamics can be reduced by choosing a gyro with a smaller characteristic time.

3. Assuming the use of a high quality gyro, noise in the gyro used to measure base motion for the feed-forward compensation does not significantly increase pointing errors.

## Appendix A

### Derivation of Dynamic Equations

This section is intended as a detailed derivation of the dynamic equations of the two-axis-gimballed beam deflector as depicted in Figure 2.

The following definitions are used in the development:

#### Coordinate Frames

V frame: i,j,k coordinates fixed to the aircraft

O frame: n,e,k coordinates fixed to the outer gimbal

M frame: r,e,d coordinates fixed to the mirror, i.e., to the inner gimbal

INERTIAL frame: inertial frame with unspecified coordinates axes

#### Notation

Superscript indicates the coordinate frame in which a vector is coordinated.

Subscript indicates the coordinate frame with regard to which derivatives are considered.

Variables

$\eta$ = Mirror azimuth angle

$\epsilon$ = Mirror elevation angle

$\omega_{V_i}, \omega_{V_j}, \omega_{V_k}$ = Aircraft angular rates about i,j,k axes, respectively.

$\omega_{O_n}, \omega_{O_e}, \omega_{O_k}$ = Outer gimbal angular rates about n,e,k axes, respectively.

$\omega_{M_r}, \omega_{M_e}, \omega_{M_d}$ = Inner gimbal (mirror) angular rates about r,e,d axes, respectively.

$B_n, B_e, B_k$ = Principal moments of inertia for outer gimbal about n,e,k axes, respectively.

$A_r, A_e, A_d$ = Principal moments of inertia for inner gimbal (mirror) about r,e,d axes, respectively.

It is assumed that gimbal axes are principal axes and that the gimbals are balanced about their respective axes of rotation.

#### Inner Gimbal Dynamics

$$\left.\frac{d}{dt}\right|_{INERTIAL} (\bar{J}_M \bar{\omega}_M) = \sum \begin{matrix}\text{Torques on the} \\ \text{inner gimbal} \\ \text{about its c.m.}\end{matrix} \qquad (A.1)$$

Applying the law of Coriolis

$$\left.\frac{d}{dt}\right|_{INERTIAL} (\bar{J}_M \bar{\omega}_M) = \left.\frac{d}{dt}\right|_M (\bar{J}_M \bar{\omega}_M) + \bar{\omega}_M \times (\bar{J}_M \bar{\omega}_M)$$

$$= \bar{J}_M \left.\frac{d}{dt}\right|_M (\bar{\omega}_M) + \bar{\omega}_M \times (\bar{J}_M \bar{\omega}_M) \qquad (A.2)$$

Writing coordinates in the I frame

$$\bar{J}_M^M = \begin{bmatrix} A_r & 0 & 0 \\ 0 & A_e & 0 \\ 0 & 0 & A_d \end{bmatrix}$$

$$\bar{\omega}_M^M = \begin{bmatrix} \omega_{M_r} \\ \omega_{M_e} \\ \omega_{M_d} \end{bmatrix}$$

$$\left\{\left.\frac{d}{dt}\right|_M \bar{\omega}_M\right\}^M = \begin{bmatrix} \dot{\omega}_{M_r} \\ \dot{\omega}_{M_e} \\ \dot{\omega}_{M_d} \end{bmatrix} \qquad (A.3)$$

$$\left\{\bar{\omega}_M \times \bar{J}_M \bar{\omega}_M\right\}^M = \begin{vmatrix} r & e & d \\ \omega_{M_r} & \omega_{M_e} & \omega_{M_d} \\ A_r\omega_{M_r} & A_e\omega_{M_e} & A_d\omega_{M_d} \end{vmatrix}$$

$$= \begin{bmatrix} (A_d - A_e)\,\omega_{M_d}\,\omega_{M_e} \\ (A_r - A_d)\,\omega_{M_r}\,\omega_{M_d} \\ (A_e - A_r)\,\omega_{M_e}\,\omega_{M_r} \end{bmatrix} \qquad (A.4)$$

Substituting (A.3) and (A.4) into (A.2)

$$\sum \text{Torques} = \begin{bmatrix} A_r \dot{\omega}_{M_r} + (A_d - A_e)\, \omega_{M_d}\, \omega_{M_e} \\ A_e \dot{\omega}_{M_e} + (A_r - A_d)\, \omega_{M_r}\, \omega_{M_d} \\ A_d \dot{\omega}_{M_d} + (A_e - A_r)\, \omega_{M_e}\, \omega_{M_r} \end{bmatrix} \quad (A.5)$$

Taking the component of (A.5) along the e axis yields (neglecting bearing friction)

$$T_e = A_e \dot{\omega}_{M_e} + (A_r - A_d)\, \omega_{M_d}\, \omega_{M_r} \quad (A.6)$$

however, due to gimbal constraint:

$$\omega_{M_r} = \omega_{0_n} \cos \varepsilon - \omega_{0_k} \sin \varepsilon \quad (A.7)$$

$$\omega_{M_d} = \omega_{0_n} \sin \varepsilon + \omega_{0_k} \cos \varepsilon \quad (A.8)$$

$$\omega_{M_r}\, \omega_{M_d} = (\omega_{0_n}^2 - \omega_{0_k}^2) \sin \varepsilon \cos \varepsilon + \omega_{0_n}\, \omega_{0_k} (\cos^2 \varepsilon - \sin^2 \varepsilon) \quad (A.9)$$

Substituting (A.9) into (A.6) yields

$$A_e \dot{\omega}_{M_e} = T_e - (A_r - A_d)\, (\omega_{0_n}^2 - \omega_{0_k}^2)\, \frac{1}{2} \sin 2\varepsilon - (A_r - A_d)\, \omega_{0_n}\, \omega_{0_k} \cos 2\varepsilon \quad (A.10)$$

Equation (A.10) describes the dynamics of the inner gimbal about the elevation axis (e axis) as a function of outer gimbal angular velocities.

<u>Outer Gimbal Dynamics</u>

$$\left.\frac{d}{dt}\right|_{\text{INERTIAL}} (\bar{J}_0 \bar{\omega}_0) = \sum \begin{matrix}\text{Torques on the} \\ \text{outer gimbal} \\ \text{about its c.m.}\end{matrix} \quad (A.11)$$

The torques on the outer gimbal are provided by the azimuth torque motor, reaction from the elevation torque motor, and by gimbal restraint from the base and from the inner gimbal.

$$\left.\frac{d}{dt}\right|_{\text{INERTIAL}} (\bar{J}_0 \bar{\omega}_0) = \bar{J}_0 \left.\frac{d}{dt}\right|_0 \bar{\omega}_0 + \bar{\omega}_0 \times \bar{J}_0 \bar{\omega}_0 \quad (A.12)$$

Writing coordinates in the G frame

$$\bar{J}_0^0 = \begin{bmatrix} B_n & 0 & 0 \\ 0 & B_e & 0 \\ 0 & 0 & B_k \end{bmatrix} \quad (A.13)$$

$$\bar{\omega}_0^0 = \begin{bmatrix} \omega_{0_n} \\ \omega_{0_e} \\ \omega_{0_k} \end{bmatrix} \quad (A.14)$$

$$\left\{ \left.\frac{d}{dt}\right|_0 \bar{\omega}_0 \right\}^0 = \begin{bmatrix} \dot{\omega}_{0_n} \\ \dot{\omega}_{0_e} \\ \dot{\omega}_{0_k} \end{bmatrix} \quad (A.15)$$

$$\left\{ \bar{\omega}_0 \times \bar{J}_0 \bar{\omega}_0 \right\}^0 = \begin{vmatrix} n & e & k \\ \omega_{0_n} & \omega_{0_e} & \omega_{0_k} \\ B_n \omega_{0_n} & B_e \omega_{0_e} & B_k \omega_{0_k} \end{vmatrix}$$

or

$$\left\{ \bar{\omega}_0 \times \bar{J}_0 \bar{\omega}_0 \right\}^0 = \begin{bmatrix} (B_k - B_e)\, \omega_{0_e}\, \omega_{0_k} \\ (B_n - B_k)\, \omega_{0_k}\, \omega_{0_n} \\ (B_e - B_n)\, \omega_{0_n}\, \omega_{0_e} \end{bmatrix} \quad (A.16)$$

Substituting (A.15) and (A.16) into (A.12)

$$\left\{ \sum \text{Torques} \right\}^0 = \begin{bmatrix} B_n \dot{\omega}_{0_n} + (B_k - B_e)\, \omega_{0_e}\, \omega_{0_k} \\ B_e \dot{\omega}_{0_e} + (B_n - B_k)\, \omega_{0_k}\, \omega_{0_n} \\ B_k \dot{\omega}_{0_k} + (B_e - B_n)\, \omega_{0_n}\, \omega_{0_e} \end{bmatrix} \quad (A.17)$$

Consider the torques on the outer gimbal along the k axis. These are:

a) The k component of the torque $\bar{T}_{MO}$ exerted by the inner gimbal on the outer gimbal.

b) $T_k$, the azimuth control torque. Now

$\overline{T}_{MO} = -\overline{T}_{OM}$ where $\overline{T}_{OM}$ is the torque exerted by the outer gimbal on the inner gimbal. $\overline{T}_{OM}$ is given by Equation (A.5) in M coordinates.

Thus the component of $\overline{T}_{MO}$ along the k axis is:

$$\overline{T}_{MO} \cdot \overline{I}_K = -A_d\dot{\omega}_{M_d} \cos\varepsilon + (A_r - A_e)\,\omega_{M_e}\omega_{M_r} \cos\varepsilon + A_r\dot{\omega}_{M_r} \sin\varepsilon + (A_d - A_e)\,\omega_{M_e}\omega_{M_d} \sin\varepsilon \tag{A.18}$$

Substituting (A.18) into (A.17)

$$B_k\dot{\omega}_{O_k} = (B_n - B_e)\omega_{O_n}\omega_{O_e} + T_k + A_r\dot{\omega}_{M_r} \sin\varepsilon + (A_d - A_e)\omega_{M_e}\omega_{M_d} \sin\varepsilon - A_d\dot{\omega}_{M_d} \cos\varepsilon + (A_r - A_e)\omega_{M_e}\omega_{M_r} \cos\varepsilon \tag{A.19}$$

Now

$$\left\{\frac{d}{dt}\bigg|_M \overline{\omega}_M\right\}^M = \begin{bmatrix} \dot{\omega}_{M_r} \\ \dot{\omega}_{M_e} \\ \dot{\omega}_{M_d} \end{bmatrix} \tag{A.20}$$

$$\left\{\frac{d}{dt}\bigg|_O \overline{\omega}_O\right\}^O \quad \begin{bmatrix} \dot{\omega}_{O_n} \\ \dot{\omega}_{O_e} \\ \dot{\omega}_{O_k} \end{bmatrix} \tag{A.21}$$

From (A.21)

$$\left\{\frac{d}{dt}\bigg|_O \overline{\omega}_O\right\}^M = \begin{bmatrix} \dot{\omega}_{O_n} \cos\varepsilon - \dot{\omega}_{O_k} \sin\varepsilon \\ \dot{\omega}_{O_e} \\ \dot{\omega}_{O_n} \sin\varepsilon + \dot{\omega}_{O_k} \cos\varepsilon \end{bmatrix} \tag{A.22}$$

$$\frac{d}{dt}\bigg|_M \overline{\omega}_M = \frac{d}{dt}\bigg|_O \overline{\omega}_M + (\overline{\omega}_O - \overline{\omega}_M) \times \overline{\omega}_M \tag{A.23}$$

Now, obviously

$$\overline{\omega}_M = \overline{\omega}_O + (\overline{\omega}_M - \overline{\omega}_O) \tag{A.24}$$

Thus

$$\frac{d}{dt}\bigg|_O \overline{\omega}_M = \frac{d}{dt}\bigg|_O \overline{\omega}_O + \frac{d}{dt}\bigg|_O (\overline{\omega}_M - \overline{\omega}_O) \tag{A.25}$$

Writing (A.25) in M frame components

$$\left\{\frac{d}{dt}\bigg|_O \overline{\omega}_M\right\}^M = \left\{\frac{d}{dt}\bigg|_O \overline{\omega}_O\right\}^M + \begin{matrix} 0 \\ \dot{\omega}_{M_e} - \dot{\omega}_{O_e} \\ 0 \end{matrix} \tag{A.26}$$

Substituting (A.22) into (A.26) yields

$$\left\{\frac{d}{dt}\bigg|_O \overline{\omega}_M\right\}^M = \begin{bmatrix} \dot{\omega}_{O_n} \cos\varepsilon - \dot{\omega}_{O_k} \sin\varepsilon \\ \dot{\omega}_{M_e} \\ \dot{\omega}_{O_n} \sin\varepsilon + \dot{\omega}_{O_k} \cos\varepsilon \end{bmatrix} \tag{A.27}$$

Now

$$(\overline{\omega}_O - \overline{\omega}_M)^M \times \overline{\omega}_M^M = \begin{vmatrix} r & e & d \\ 0 & \omega_{O_e} - \omega_{M_e} & 0 \\ \omega_{O_n}\cos\varepsilon - \omega_{O_k}\sin\varepsilon & \omega_{M_e} & \omega_{O_n}\sin\varepsilon + \omega_{O_k}\cos\varepsilon \end{vmatrix} \tag{A.28}$$

Substituting (A.28) and (A.27) into (A.23) yields

$$\dot{\omega}_{M_r} = \dot{\omega}_{O_n}\cos\varepsilon - \dot{\omega}_{O_k}\sin\varepsilon + \omega_{O_e}\omega_{O_n}\sin\varepsilon + \omega_{O_e}\omega_{O_k}\cos\varepsilon - \omega_{M_e}\omega_{M_n}\sin\varepsilon - \dot{\omega}_{M_e}\omega_{O_k}\cos\varepsilon \tag{A.29}$$

Similarly

$$\dot{\omega}_{M_d} = \dot{\omega}_{O_n}\sin\varepsilon + \dot{\omega}_{O_k}\cos\varepsilon - \omega_{O_e}\omega_{O_n}\cos\varepsilon + \omega_{O_e}\omega_{O_k}\sin\varepsilon + \omega_{M_e}\omega_{O_n}\cos\varepsilon - \omega_{M_e}\omega_{O_k}\sin\varepsilon \tag{A.30}$$

Substituting (A.29) and (A.30) into (A.19) yields

$$B_k \dot{\omega}_{O_k} =$$

$$(B_n - B_e)\,\omega_{O_n}\omega_{O_e} + T_k$$

$$+A_r\dot{\omega}_{O_n}\cos\varepsilon\sin\varepsilon - A_r\dot{\omega}_{O_k}\sin^2\varepsilon + A_r\omega_{O_e}\omega_{O_n}\sin^2\varepsilon$$

$$+A_r\omega_{O_e}\omega_{O_k}\sin\varepsilon\cos\varepsilon - A_r\omega_{M_e}\omega_{O_n}\sin^2\varepsilon - A_r\omega_{M_e}\omega_{O_k}\sin\varepsilon\cos\varepsilon$$

$$- A_d\dot{\omega}_{O_n}\sin\varepsilon\cos\varepsilon - A_d\dot{\omega}_{O}\cos^2\varepsilon + A_d\omega_{O_e}\omega_{O_n}\cos^2\varepsilon$$

$$- A_d\omega_{O_e}\omega_{O_k}\sin\varepsilon\cos\varepsilon - A_d\omega_{M_e}\omega_{O_n}\cos^2\varepsilon$$

$$+ A_d\omega_{M_e}\omega_{O_k}\sin\varepsilon\cos\varepsilon + A_d\omega_{M_e}\omega_{M_d}\sin\varepsilon$$

$$+ A_r\omega_{M_e}\omega_{M_r}\cos\varepsilon - A_e\omega_{M_e}(\omega_{M_d}\sin\varepsilon + \omega_{M_r}\cos\varepsilon) \qquad (A.31)$$

Now

$$\omega_{M_d} = \omega_{O_n}\sin\varepsilon + \omega_{O_k}\cos\varepsilon \qquad (A.32)$$

$$\omega_{M_r} = \omega_{O_n}\cos\varepsilon - \omega_{O_k}\sin\varepsilon \qquad (A.33)$$

Substituting (A.32) and (A.33) into (A.31) yields

$$(B_k + A_r\sin^2\varepsilon + A_d\cos^2\varepsilon)\,\dot{\omega}_{O_k} = T_k$$

$$+(B_n - B_e)\omega_{O_n}\omega_{O_e} + A_r\dot{\omega}_{O_n}\cos\varepsilon\sin\varepsilon + A_r\omega_{O_e}\omega_{O_n}\sin^2\varepsilon$$

$$+ A_r\omega_{O_e}\omega_{O_k}\sin\varepsilon\cos\varepsilon - A_r\omega_{M_e}\omega_{O_n}\sin^2\varepsilon$$

$$- A_r\omega_{M_e}\omega_{O_k}\sin\varepsilon\cos\varepsilon - A_d\dot{\omega}_{O_n}\sin\varepsilon\cos\varepsilon$$

$$+ A_d\omega_{O_e}\omega_{O_n}\cos^2\varepsilon - A_d\omega_{O_e}\omega_{O_k}\sin\varepsilon\cos\varepsilon$$

$$- A_d\omega_{M_e}\omega_{O_n}\cos^2\varepsilon + A_d\omega_{M_e}\omega_{O_k}\sin\varepsilon\cos\varepsilon$$

$$+ A_d\omega_{M_e}(\omega_{O_n}\sin^2\varepsilon + \omega_{O_k}\sin\varepsilon\cos\varepsilon)$$

$$+ A_r\omega_{M_e}(\omega_{O_n}\cos^2\varepsilon - \omega_{O_k}\sin\varepsilon\cos\varepsilon)$$

$$- A_e\,\omega_{M_e}\,\omega_{O_n} \qquad (A.34)$$

Again rearranging (A.34) produces

$$(B_k + A_r\sin^2\varepsilon + A_d\cos^2\varepsilon)\dot{\omega}_{O_k} = T_k$$

$$+ (B_n - B_e + A_r\sin^2\varepsilon + A_d\cos^2\varepsilon)\omega_{O_n}\omega_{O_e}$$

$$- (A_e - A_r\cos 2\varepsilon + A_d\cos 2\varepsilon)\omega_{O_n}\omega_{M_e}$$

$$+ (A_d - A_r)\sin\varepsilon\cos\varepsilon\, 2\,\omega_{M_e}\omega_{O_k}$$

$$- (A_d - A_r)\sin\varepsilon\cos\varepsilon\,\omega_{O_e}\omega_{O_k}$$

$$- (A_d - A_r)\sin\varepsilon\cos\varepsilon\,\dot{\omega}_{O_n} \qquad (A.35)$$

Now,

$$\left\{\frac{d}{dt}\bigg|_O \bar{\omega}_O\right\}^O = \begin{bmatrix}\dot{\omega}_{O_n}\\ \dot{\omega}_{O_e}\\ \dot{\omega}_{O_k}\end{bmatrix} \qquad (A.36)$$

$$\left\{\frac{d}{dt}\bigg|_V \bar{\omega}_V\right\}^V = \begin{bmatrix}\dot{\omega}_{V_i}\\ \dot{\omega}_{V_j}\\ \dot{\omega}_{V_k}\end{bmatrix} \qquad (A.37)$$

$$\left\{\frac{d}{dt}\bigg|_V \bar{\omega}_V\right\}^O = \begin{bmatrix}\dot{\omega}_{V_i}\cos\eta + \dot{\omega}_{V_j}\sin\eta\\ -\dot{\omega}_{V_i}\sin\eta + \dot{\omega}_{V_j}\cos\eta\\ \dot{\omega}_{V_k}\end{bmatrix} \qquad (A.38)$$

Now

$$\frac{d}{dt}\bigg|_O \bar{\omega}_O = \frac{d}{dt}\bigg|_V \bar{\omega}_O + (\bar{\omega}_V - \bar{\omega}_O)\times\bar{\omega}_O \qquad (A.39)$$

Again, obviously

$$\bar{\omega}_O = \bar{\omega}_V + (\bar{\omega}_O - \bar{\omega}_V) \qquad (A.40)$$

Thus

$$\frac{d}{dt}\bigg|_V \bar{\omega}_O = \frac{d}{dt}\bigg|_V \bar{\omega}_V + \frac{d}{dt}\bigg|_V (\bar{\omega}_O - \bar{\omega}_V) \qquad (A.41)$$

Writing (A.41) in O frame components

$$\left\{\frac{d}{dt}\bigg|_V \bar{\omega}_O\right\}^O = \left\{\frac{d}{dt}\bigg|_V \bar{\omega}_V\right\}^O + \begin{bmatrix} 0 \\ 0 \\ \dot{\omega}_{O_k} - \dot{\omega}_{V_k} \end{bmatrix} \quad (A.42)$$

Substituting (A.38) into (A.42) yields

$$\left\{\frac{d}{dt}\bigg|_V \bar{\omega}_O\right\}^O = \begin{bmatrix} \dot{\omega}_{V_i} \cos\eta + \dot{\omega}_{V_j} \sin\eta \\ -\dot{\omega}_{V_i} \sin\eta + \dot{\omega}_{V_j} \cos\eta \\ \dot{\omega}_{O_k} \end{bmatrix} \quad (A.43)$$

Now

$$(\bar{\omega}_V - \bar{\omega}_O)^O \times \bar{\omega}_O^O = \quad (A.44)$$

$$\begin{vmatrix} n & e & k \\ 0 & 0 & \omega_{V_k} - \omega_{O_k} \\ \omega_{V_i}\cos\eta + \omega_{V_j}\sin\eta & -\omega_{V_i}\sin\eta + \omega_{V_j}\cos\eta & \omega_{V_k} \end{vmatrix}$$

Substituting (A.44) and (A.43) into (A.40) produces

$$\dot{\omega}_{O_n} = \dot{\omega}_{V_i} \cos\eta + \dot{\omega}_{V_j} \sin\eta \quad (A.45)$$

$$+ \omega_{V_i}\omega_{V_k} \sin\eta - \omega_{V_j}\omega_{V_k} \cos\eta$$

$$- \omega_{V_i}\omega_{O_k} \sin\eta + \omega_{V_j}\omega_{O_k} \cos\eta$$

Also

$$\omega_{O_e} = -\omega_{V_i} \sin\eta + \omega_{V_j} \cos\eta \quad (A.46)$$

Substituting (A.45) and (A.46) into (A.35) yields

$$(B_k + A_r \sin^2\varepsilon + A_d \cos^2\varepsilon)\,\dot{\omega}_{O_k} =$$

$$T_k + (B_n - B_e + A_r \sin^2\varepsilon + A_d \cos^2\varepsilon)\,\omega_{O_n}\omega_{O_e}$$

$$- (A_e - A_r\cos 2\varepsilon + A_d\cos 2\varepsilon)\omega_{O_n}\omega_{M_e} + (A_d - A_r)\sin\varepsilon\cos\varepsilon\, 2\omega_{M_e}\omega_{O_k}$$

$$- (A_d - A_r)\sin\varepsilon\cos\varepsilon \Big\{\dot{\omega}_{V_i}\cos\eta + \dot{\omega}_{V_j}\sin\eta + \omega_{V_i}\omega_{V_k}\sin\eta$$

$$- \omega_{V_j}\omega_{V_k}\cos\eta - 2\omega_{V_i}\omega_{O_k}\sin\eta + 2\omega_{V_j}\omega_{O_k}\cos\eta\Big\} \quad (A.47)$$

Equation (A.47) describes the dynamics of the beam deflector about the k axis in terms of base motion and motion of the beam deflector about the k and e axes.

## Appendix B

### Disturbance Input Relationships

The disturbance inputs to the elevation loop, $T_{d_e}$ and $\omega_{O_e}$, and those to the azimuth loop, $T_{d_a}$ and $\omega_{O_n}$, can be written in terms of base motion and required line-of-sight rates by noting:

$$\omega_{O_n} = \omega_{V_i} \cos\eta + \omega_{V_j} \sin\eta \quad (B.1)$$

$$\omega_{O_e} = -\omega_{V_i} \sin\eta + \omega_{V_j} \cos\eta \quad (B.2)$$

Substitution of (B.1) and (B.2) into (A.10) and (A.47) results in all disturbances expressed in terms of base motion rates and required line-of-sight tracking rates.

In order to determine the PSD of the pointing error, it is necessary to know the PSD's of the various disturbance inputs. This can be readily accomplished knowing the PSD of each component of base motion and required tracking rates if independence is assumed amongst the various angular velocity components.

As an example of the determination of PSD consider the disturbance input term $\omega_{V_i}\omega_{V_j}$.

The PSD for $\omega_{V_i}$ or $\omega_{V_j}$ is given by Equation (2).

Assuming independence, it is directly shown that

$$R_{\omega_{V_i}\omega_{V_j}}(\tau) = R_{\omega_{V_i}}(\tau)\, R_{\omega_{V_j}}(\tau) \quad (B.3)$$

where $R_z(\tau)$ is the autocorrelation of the variable z.

Taking the inverse Fourier transform of Equation (2) yields

$$R_{\omega_{V_i}}(\tau) = R_{\omega_{V_j}}(\tau) \approx 0.1 \left\{\frac{e^{-1.5|\tau|}}{3} - \frac{e^{-1400|\tau|}}{2800}\right\} \quad (B.4)$$

Substituting (B.4) into (B.3) and taking the Fourier transform yields

$$\Phi_{\omega_{V_i}\omega_{V_j}}(\omega) = 0.01\left\{\frac{.6667}{\omega^2 + 3^2} - \frac{.6674}{\omega^2 + 1401.5^2}\right\} \tag{B.5}$$

The PSD for other disturbance inputs is similarly developed.

REFERENCES


1. Whitaker, J.L., and Burdin, C., A Gyro Stabilized Heliostat for Airborne Astronomy, ISA Transactions, Vol 5, No 2, 1966.

2. Rue, A.K., Stabilization of Precision Electrooptical Pointing and Tracking Systems, IEEE Transactions on Aerospace and Electronic Systems, Vol AES-5, No 5, September 1969.

3. Wrigley, W., Single-Degree-of-Freedom-Gyroscopes, Report R-375, MIT Draper Laboratory, Cambridge, Mass.; July, 1962.

4. Lichtenstein, P.E., Gyros, Platforms, Accelerometers, Technical Information for the Engineer, Kearfott Division, General Precision, Inc., June, 1963.

5. Truncale, A., Koenigsberg, W., and Harris, R., Spectral Density Measurements of Gyro Noise, MIT Draper Laboratory, Report E-2641, Cambridge, Mass.; February 1972.

6. Weinstock, H., Design of a Precision Tilt and Vibration Isolation System, NASA TR R-281 NASA Electronics Research Center, Cambridge, Mass., March 1968.

7. Results of Tests on Systron-Doller Angular Accelerometer performed by General Electric, Space Systems Organization, Valley Forge Space Center, Pa., 10 July 1970.